Journal of Solid State Chemistry 187 (2012) 225–230

Contents lists available at SciVerse ScienceDirect

Journal of Solid State Chemistry

journal homepage: www.elsevier.com/locate/jssc

Structural and magnetic characterisation of $CoSb_2O_4$, and the substitution of Pb^{2+} for Sb^{3+}

Benjamin P. de Laune, Colin Greaves *

School of Chemistry, University of Birmingham, Birmingham B15 2TT, UK

ARTICLE INFO

Article history:
Received 15 November 2011
Received in revised form
14 January 2012
Accepted 16 January 2012
Available online 24 January 2012

Keywords:
Cobalt antimony oxide
$CoSb_2O_4$
Magnetic structure
Pb substitution

ABSTRACT

The nuclear and magnetic structures of the synthetic schafarzikite related material $CoSb_2O_4$ have been determined from neutron powder diffraction data. The compound is tetragonal ($P4_2/mbc$) with refined lattice constants at 300 K of, $a=8.49340(9)$ Å, $c=5.92387(8)$ Å. The magnetic ordering is shown to be consistent with a C mode with moments aligned along [0 0 1]. Magnetic susceptibility measurements indicate a canted antiferromagnetic ground state, for which the ferromagnetic component shows unusually high coercivity. The thermal stability of $CoSb_2O_4$ in air is reported. The substitution of Pb^{2+} for Sb^{3+} has been investigated and found to cause oxidation of both Co^{2+} to Co^{3+} and Sb^{3+} to Sb^{5+}.

1. Introduction

The susceptibility of Sb(III) to oxidation to Sb(V) in oxide environments provides high thermal stability only to ternary Co–Sb–O oxides with antimony in its higher oxidation state. However, under stringent synthetic conditions, $CoSb_2O_4$ can be formed, which is a member of the MSb_2O_4 family with M=Mn, Fe, Co, Ni and Zn [1–5]. The structural details for most of the MSb_2O_4 materials have been reported including those for the naturally occurring parent phase Schafarzikite ($FeSb_2O_4$). All variants are tetragonal with spacegroup $P4_2/mbc$, and contain chains of edge-linked MO_6 octahedra running along [0 0 1]; the chains are connected via trigonal pyramidal SbO_3 units, as shown in Fig. 1. All MSb_2O_4 phases have been shown to display antiferromagnetic ordering with Neel temperatures in the range 40–60 K [1,2,6] and a transition of the magnetic modal ordering from a predominant A mode to a C mode (vide infra) on crossing the first row transition metals: $FeSb_2O_4$ and $MnSb_2O_4$ display A-type order whereas $NiSb_2O_4$ exhibits a C-type arrangement. Unfortunately, no detailed crystallographic and magnetic structures have been reported for $CoSb_2O_4$, such that it is unclear where the magnetic transition occurs, and rationalisation of the different magnetic structures is incomplete.

The edge sharing nature of the octahedra, forming infinite straight chains along [0 0 1] (Fig. 1), provides three magnetic communication pathways between transition metal cations: intrachain direct exchange and superexchange and interchain superexchange; these are summarised well by Witteveen [7]. The A and C magnetic modes of $MnSb_2O_4$ and $NiSb_2O_4$ are shown in Fig. 2, as are the remaining possible spin arrangements that the Schafarzikite system can, in principle, adopt. The C modal ordering, with parallel intrachain moments, as found in $NiSb_2O_4$, is attributed to a dominant 90° superexchange taking place between adjacent transition metal sites through a common O^{2-} edge of the octahedra where full occupation of the t_{2g} orbitals prevents direct exchange from occurring. On the other hand, in the Mn system a dominant A mode is observed that can be rationalised by a strong direct exchange mechanism taking place where satisfaction of the Pauli principle with decreased interatomic separation (greater orbital overlap) gives rise to the observed antiparallel intrachain interactions. Interestingly, the moments for the A-type $MnSb_2O_4$ are perpendicular to [0 0 1], whereas in C-type $NiSb_2O_4$, the moments align along [0 0 1].

The ability of the structure to allow substitution of Pb^{2+} cations on the Sb^{3+} site has been demonstrated for the Mn [8] and Fe [9] variants, but with different charge balance mechanisms. Such substitutions are of great potential interest providing chemical control of the oxidation state of the transition metal ion, and hence the magnetic and electrical properties of the system. It was found that for the manganese system, the high stability of Mn^{2+} to oxidation resulted in the preferential oxidation of Sb^{3+} to Sb^{5+}, which in turn substituted for Mn^{2+} in the octahedral chains and resulted in impure products. This is in stark contrast to the finding of Whitaker et al. [9], where a similar experiment

* Corresponding author. Fax: +44 121 414 4442.
E-mail address: c.greaves@bham.ac.uk (C. Greaves).

0022-4596/$ - see front matter © 2012 Elsevier Inc. All rights reserved.
doi:10.1016/j.jssc.2012.01.032

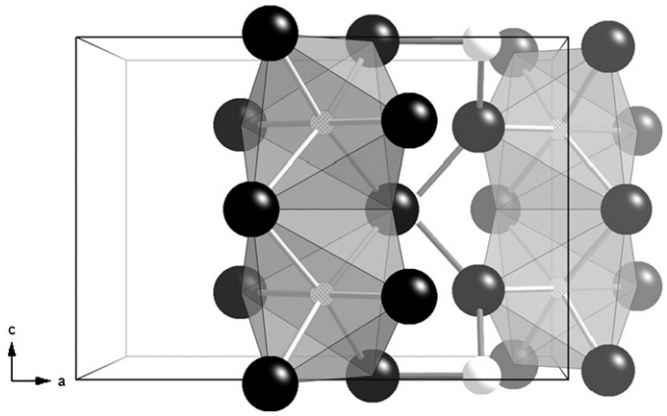

Fig. 1. Part of the structure of $CoSb_2O_4$ viewed approximately along [0 1 0] showing the interconnectivity of the edge sharing octahedra via the bridging trigonal pyramidal Sb^{3+} ions. Grey, black and cross hatched spheres represent: Sb^{3+}, O^{2-} and Co^{2+}, respectively.

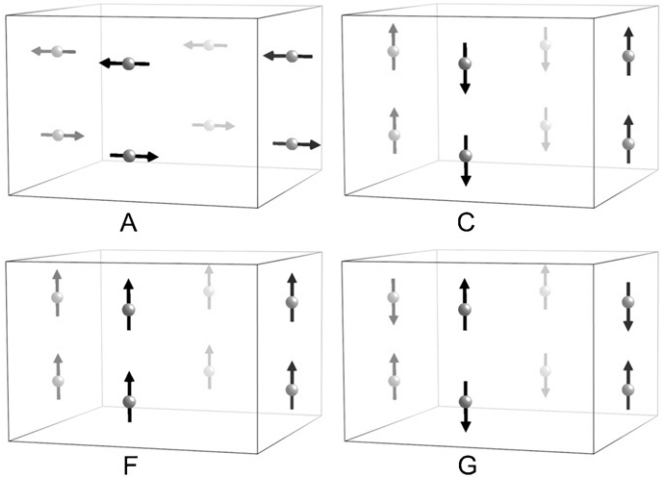

Fig. 2. The four possible spin alignments for the Schafarzikite system giving rise to the A mode (spins along *x*, e.g., $MnSb_2O_4$), C mode (spins along *z*, e.g., $NiSb_2O_4$), G, and F modes.

based on the iron variant found that substituting Sb^{3+} with varying levels of Pb^{2+} created a pure single phase where charge balance was based solely on the oxidation of Fe^{2+} to Fe^{3+}.

Here we report a Neutron Powder Diffraction (NPD) study of the nuclear and magnetic structure of $CoSb_2O_4$. We also present results on the possible synthesis of $CoSb_{1.5}Pb_{0.5}O_4$, a mixed Co^{2+}/Co^{3+} phase.

2. Experimental

$CoSb_2O_4$ was synthesised by heating an intimately ground mixture of CoO (325 mesh, Aldrich) and Sb_2O_3 (99%, ReagentPlus, 5micron powder, Aldrich) within an alumina crucible which was in turn contained within an evacuated quartz tube for two 6 h periods at 700 °C with intermittent grinding. Reagents were dried prior to use by heating at 350 °C under dynamic vacuum.

Lead doped samples were synthesised by heating mixtures of CoO, Co_3O_4 (Sigma–Aldrich $<10\,\mu$), PbO (Puriss. p.a. $\geq 99.0\%$, Sigma–Aldrich,) and Sb_2O_3 to produce a composition of $CoSb_{1.5}Pb_{0.5}O_4$, in an analogous fashion to $CoSb_2O_4$. Alumina inserts were found to be important for minimising sample degradation.

X-ray powder diffraction (XRPD) data were collected on a Bruker D8 diffractometer in transmission geometry, (PSD: Lynxeye, Cu $K_{\alpha 1}$, Ge monochromator). NPD patterns were recorded on the D2B diffractometer at the Institut Laue-Langevin (ILL) at 300 K and 4 K using 8 mm diameter vanadium cans. Liquid He temperatures were achieved using a Displex cryocooler. Monochromatic neutrons of 1.5918 Å (calibrated using XRPD data from the same $CoSb_2O_4$ sample) were used. Electronic deconvolution of the detected beam into its full width (high intensity) and central detector portion (lower intensity but greater peak symmetry and resolution) were examined in the structural analysis. Nuclear neutron scattering lengths of 0.249, 0.581, 0.557 and 0.940 (all $\times 10^{-14}$ m) were assigned to Co, O, Sb and Pb, respectively. Magnetic susceptibility measurements were recorded on a Quantum Design superconducting quantum interference device (SQUID) magnetometer under Field Cooled (FC) and Zero Field Cooled (ZFC) conditions; applied fields of 10, 100 and 1000 Oe were investigated between 5 K and 300 K at a heating and cooling rate of 10 K/min; no correction for diamagnetism was applied. The polycrystalline samples (~50 mg) were contained in a capsule, where sample movement was suppressed with PTFE tape. Powder patterns were indexed using the programme DICVOL06 [10] whilst both crystal and magnetic structures were refined using the General Structures Analysis System (GSAS) [11] with the EXPGUI interface [12]. Bond valence sums (BVS) were calculated using the parameters of Brown and Altermatt [13]. Thermogravimetric Analysis (TGA) and Differential Thermal Analysis (DTA) measurements were made on a Netzsch Sta 449 F1 analyser in an atmosphere of oxygen and a heating rate of 10 °C min^{-1}.

3. Results and discussion

3.1. Crystallographic and magnetic structures

The XRPD pattern of $CoSb_2O_4$ was indexed on a single tetragonal cell where the general reflection conditions for the space group $P4_2/mbc$ were satisfied in accordance with previous reports for Schafarzikite related systems [2,3]. Rietveld analysis of the NPD data proceeded in accordance with $P4_2/mbc$ symmetry; both the high intensity and higher resolution NPD data sets were analysed, but the higher resolution data provided better profile analysis and easier identification of any impurity phase during the Rietveld refinement. A small CoO impurity (~3 wt%, from NPD data) was identified in both the neutron and X-ray data sets, and therefore nuclear (300 K and 4 K) and magnetic (4 K) contributions from CoO were included in the NPD refinements. The background was refined using the shifted Chebyschev function, and a correction for preferred orientation along [0 0 1] was applied for the XRPD data. The results for the final NPD fit are shown in Table 1 and Fig. 3 ($\chi^2=2.606$, $R_{wp}=0.0493$, 33 variables, 300 K) where all isotropic displacement parameters (IDPs) and atomic positions were refined independently. For comparison, the lattice parameters obtained from the XRPD refinement ($\chi^2=1.924$, $R_{wp}=0.0471$, $a=8.49285(7)$ Å, $c=5.92449(5)$ Å), where all IDPs and atomic positions were refined independently, show small but significant differences from those reported by Koyama et al. ($a=8.500(1)$ Å, $c=5.931(1)$ Å) [4]. The sample colour, pinkish brown, is similar to that reported [4] and reflects the octahedral coordination of divalent cobalt.

On cooling to 4 K, no peak broadening of the nuclear phase was observed suggesting retention of the original symmetry. The emergence of new intense reflections at low angle could be indexed for a cell consistent with the nuclear lattice constants and were attributed to reflections from magnetic ordering of the system. The magnetic scattering was analysed using the Co^{2+} form factor and a second magnetic only phase, spacegroup *P*1, in order to provide full flexibility for the magnetic structure. The dominant observed magnetic peaks at 10.828°, 24.285°,

Table 1
Atomic positions, fractional occupancies, IDPs, statistics and lattice parameters obtained from least squares analysis of the NPD data for $CoSb_2O_4$ at 300 and 4 K.

		$CoSb_2O_4$	
		300 K	4 K
Co, 4d	$100 \times U_{iso}$ (Å^2)	0.76(7)	0.04(9)
Sb, 8h	(x, y, 0)	0.1750(2), 0.1644(1)	0.1749(2), 0.1639(2)
	$100 \times U_{iso}$ (Å^2)	0.84(3)	0.04(3)
O1, 8h	(x, y, 0)	0.0985(1), 0.6391(1)	0.0978(2), 0.6392(2)
	$100 \times U_{iso}$ (Å^2)	0.96(3)	0.09(3)
O2, 8g	(x, y, 0.25)	0.6791(1), 0.1791(1)	0.6787(1), 0.1787(1)
	$100 \times U_{iso}$ (Å^2)	1.42(2)	0.18(3)
χ^2, R_{wp}, R_F^2		2.606, 0.0493, 0.0461	2.881, 0.0580, 0.0425
a/Å		8.49340(9)	8.4809(1)
c/Å		5.92387(8)	5.92092(9)

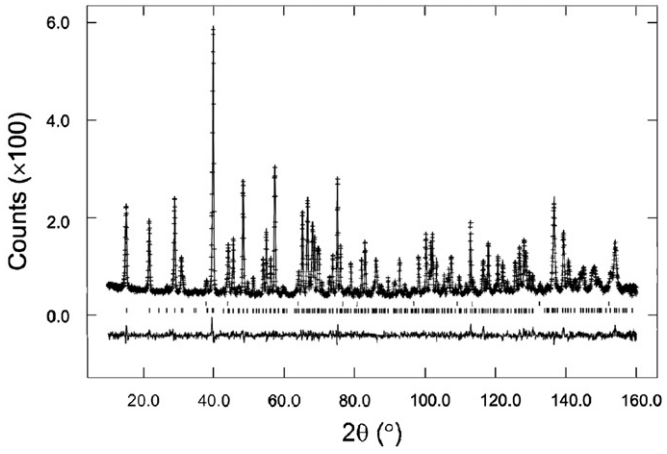

Fig. 3. The Final Rietveld refinement plots of $CoSb_2O_4$ based on 300 K NPD data using $P4_2/mbc$: observed data (+), calculated and difference profiles (continuous lines) and, from the bottom, reflection positions (|) of $CoSb_2O_4$ and CoO nuclear structures, respectively.

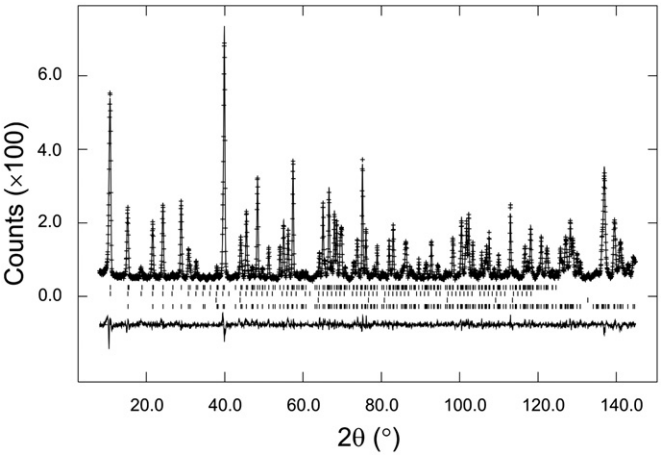

Fig. 4. Rietveld refinement of $CoSb_2O_4$ based on 4 K NPD data using $P4_2/mbc$: observed data (+), calculated and difference profiles (continuous lines) and, from the bottom, reflection positions (|) of $CoSb_2O_4$ and CoO nuclear structure followed by CoO and $CoSb_2O_4$ (Top) magnetic structures, respectively.

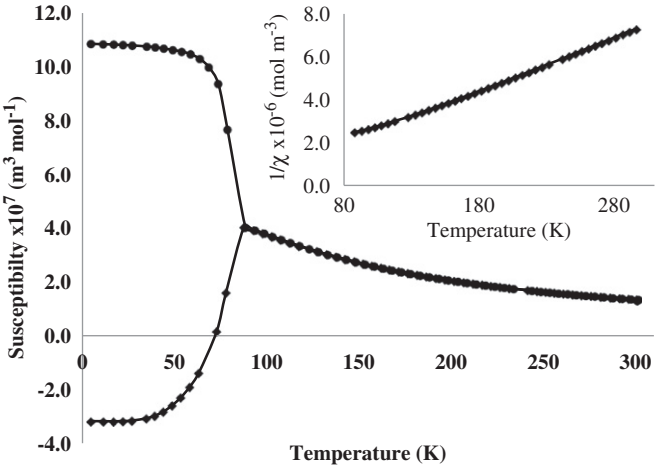

Fig. 5. Magnetic susceptibility plots for $CoSb_2O_4$, FC (●), ZFC (♦); applied field of 100 Oe. Inset: inverse susceptibility clearly showing deviation from linearity below 140 K.

32.762°, and 39.613° 2θ, ((100), (210), (300) and (320), respectively), suggested C-type magnetic order with intrachain ferromagnetic coupling and inter-chain antiferromagnetic coupling (Fig. 2).

Refinement based on a spin alignment along [0 0 1] gave a significantly better fit to the data than other possible orientations. However, a small component of spin in the xy plane is possible. The magnetic structure which gave the most stable refinement (Fig. 4, χ^2=2.881, R_{wp}=0.0580, 35 variables, 4 K, a=8.4809(1) Å, c=5.92092(9) Å) for the $CoSb_2O_4$ system is given by a C mode orientated solely along the primary z-axis (Fig. 2). The refined magnitude of each moment 3.73(2) μ_B is substantially larger than the expected moment ($2S$=3 μ_B) and implies a large orbital contribution to the overall moment, as expected for the $^4T_{1g}$ ground state for purely octahedral Co^{2+} ions. The enhanced moment is consistent with other NPD studies of octahedral Co^{2+} containing compounds, e.g., $CoTa_2O_6$ ($\mu=3.25\pm0.02$ μ_B), [14] and $CoSO_4$ ($\mu=3.3\pm0.2$ μ_B) [15] but the orbital contribution in $CoSb_2O_4$ is clearly large. The magnetic order inferred from the NPD data corresponds with space group $P4_2'/mbc'$.

The structure is consistent with those previously reported for MSb_2O_4 phases, and comprises chains of distorted edge sharing octahedra propagating along [0 0 1] where the individual octahedra are orientated such that the apical (Co–O2) bonds lie perpendicular to [0 0 1], and are directed towards the adjacent chain (Fig. 1). On cooling, the unit cell is seen to contract along both a and c, where the Co–O_{ap} bonds shorten twice as much as the Co–O_{eq} bonds (Table 3); however, the opposite is seen in the Sb–O bonds in which a small extension of all bonds is observed on cooling. The room temperature distorted octahedral environment is similar to that of $ZnSb_2O_4$, where comparable O1–Zn–O1 angles determined by single crystal X-ray diffraction are 88.6(1)°, 165.4(2)°, and 93.3(1)° [16]. Bond valence sum calculations based on the room temperature data (+2.015 and +3.015 for Co and Sb, respectively) show the model to be compatible with the bonding requirements of Co^{2+} and Sb^{3+}.

Magnetic susceptibility measurements under FC and ZFC conditions highlighted some unusual results. The susceptibility plot (Fig. 5) shows behaviour consistent with a canted antiferromagnetic system, with divergence of FC and ZFC data at the magnetic ordering temperature; the ferromagnetic component was too small to be observed in the NPD data. Similar canting has been observed for Pb-substituted $FeSb_2O_4$ [9] and suggests that the true symmetry of the magnetically ordered phase may be orthorhombic. The highly unusual negative response in the ZFC run was at first believed to be an instrumental artifact; however, we now believe it to be consistent with the findings of Kumar

et al. [17] who showed that small trapped fields within the superconducting magnet, under zero applied field conditions, influence the magnetisation of $CoCr_2O_4$. This feature was probed in the present study by the application of fields of 2 T or −2 T after sample centring but immediately before commencing a ZFC run. No external field was applied during measurement acquisition on warming. The findings (Fig. 6) show that when the sample is cooled where the previously applied field was positive the sample response was negative (−0.00736 emu/g at 5 K) and the opposite is observed when a negative field was initially applied (0.00797 emu/g at 5 K). This suggests that setting the field to zero Oe leaves behind a very small trapped field (flux) within the superconducting magnet, whose sign opposes the previously applied field, resulting in ZFC measurements actually being FC in a non-zero field. Although the field is very small, it has a noticeable effect on this particular sample. ZFC–FC measurements taken at 10, 100 and 1000 Oe where the previous applied field was 100 Oe during centring showed that the negative response due to the trapped field was only removed at 5 K when the applied filed exceeded 100 Oe. These findings, significantly, demonstrate the high coercivity of the small canted ferromagnetic component of this material.

The material shows Curie–Weiss behaviour at high temperatures (160–300 K), for which the Co^{2+} effective moment is calculated to be 5.06 μ_B and $\theta = 3.28 \pm 1$ K consistent with high spin Co^{2+} with a large orbital contribution to the moment (spin-only moment 3.87 μ_B) and weak overall ferromagnetic exchange. However, at lower temperatures (below 140 K), a deviation from linearity is clearly seen (Fig. 5, inset) indicative of enhanced antiferromagnetic interactions and consistent with the resultant antiferromagnetic ground state. The Neel temperature obtained from measurements taken under temperature settle conditions (T_N=79 K) is found to be significantly greater than that of its analogues ($FeSb_2O_4$=45 K [9] and $NiSb_2O_4$=47.0(5) K [7]) indicating stronger magnetic interactions.

The Co^{2+} magnetic moment clearly requires a high spin configuration. Based on the relationship $c/2$=Co–Co distance, the inter-transition metal separation distance along [0 0 1] is calculated as 2.960 Å (4 K) where Fe–Fe=2.952 Å (4 K) and Ni–Ni=2.950 Å (2 K) based on values previously reported [9,18]. The larger Co–Co distance provides a possible basis for explaining the change in modal ordering. It is expected that the increase in M–M intrachain separation would result in a reduction in the strength of the direct exchange, and allow dominance of the 90° superexchange mechanism and the corresponding transition from an A mode ground state in $FeSb_2O_4$, to C mode for the Co variant. Given the similar interatomic distance for the iron and nickel variants, the different ordering relates to the full t_{2g} orbitals in the nickel system that prevents any direct exchange.

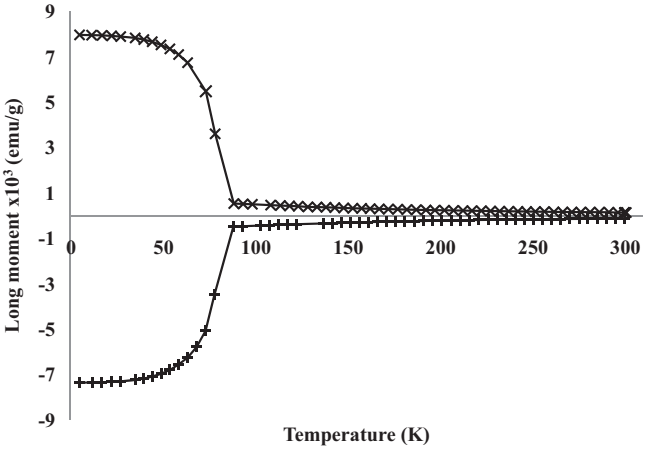

Fig. 6. ZFC measurements taken in the absence of an externally applied field, where a large positive or negative field was applied for 60 s and then set to 0 Oe prior to commencing a ZFC run. The (+) and (×) refer to the measurements made where a 2 T field and −2 T field were applied prior to scan commencement.

3.2. TGA analysis

Resistance of $CoSb_2O_4$ to oxidation was investigated using TGA in an oxygen atmosphere, and discovered to be appreciable. No oxygen uptake is seen to occur below 500 °C (Fig. 7), but rapid oxygen uptake occurs between 550 °C and 650 °C. One large exotherm is seen coinciding with the mass increase, indicating a single phase change, which can be attributed to the oxidation of $CoSb_2O_4$ to $CoSb_2O_6$, and was verified by XRPD.

3.3. Synthesis of $CoSb_{1.5}Pb_{0.5}O_4$

The substitution of Pb^{2+} for Sb^{3+} in $MnSb_2O_4$ and $FeSb_2O_4$ has provided different mechanisms for charge balance although the Schafarzikite structure was maintained [8,9]. Only for $FeSb_2O_4$ did the lead substitution allow control of the transition metal oxidation state. Attempts to synthesise pure samples of $CoSb_{1.5}Pb_{0.5}O_4$ proved very difficult, and all heating and cooling regimes provided samples contaminated with the spinel $Co(Co_{1.33}Sb_{0.66})O_4$, which implied that the main phase was cobalt deficient. No evidence was observed for a lead containing impurity. The main phase was indexed for a tetragonal cell and refinement of the NPD data at 300 K and 4 K (high resolution data sets) proceeded using $P4_2/mbc$ symmetry and the atomic coordinates obtained from the $CoSb_2O_4$ refinement. Nuclear and magnetic contributions of the spinel impurity were included in the refinements. At first, an idealised model based on the oxidation of cobalt only, where Sb and Pb were constrained to possess the same atomic coordinates and thermal parameters (initially set to 0.025), was tested for the 300 K data set. Occupancies were set to be consistent with the composition $CoSb_{1.5}Pb_{0.5}O_4$. The fit, where only the atomic coordinates, phase fractions, cell and profile parameters were refined (χ^2=3.301, R_{wp}=0.0518 a=8.4826(2) Å, c=6.0543(3) Å) demonstrated a satisfactory refinement where elemental occupancies from the closely matching peak intensities (impurity ≈ 11 wt %) appeared consistent with stoichiometry. The increase in the c parameter and decrease in a compared with $CoSb_2O_4$ are consistent with the results of Pb substitution into $FeSb_2O_4$ [9], and are suggestive of cation oxidation within the octahedral chains. However, when varying the IDPs, cobalt returned an anomalously small value ($100 \times U_{iso}$=0.09(9) Å^2 compared with approximately 2.40 Å^2 for all other sites), which suggested the possible substitution of the more heavily scattering Sb into the chains. For this

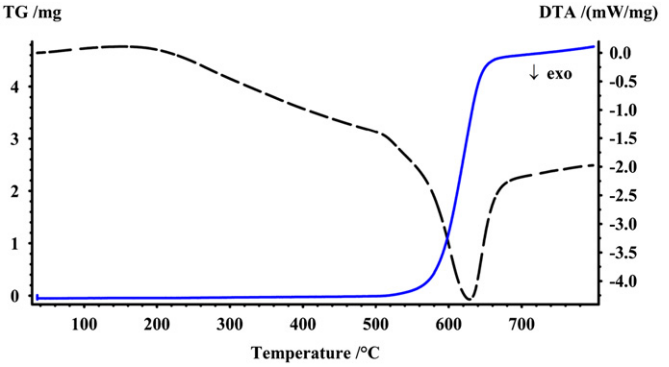

Fig. 7. TGA analysis of $CoSb_2O_4$; solid line and dashed line represent mass change and enthalpy change, respectively.

model, $\chi^2=2.770$, $R_{wp}=0.0474$, for 31 variables. It therefore seemed likely that oxidation of some Sb^{3+} to Sb^{5+} was occurring to create $(Co_{1-x}Sb_x)(Sb_{1-y}Pb_y)_2O_4$; this is similar to results for the manganese system [8]. A model was therefore explored based on the extreme situation where only oxidation of antimony was allowed, and the Pb content was increased to accord with the presence of pure $Co(Co_{1.33}Sb_{0.66})O_4$ impurity. A constraint was applied which maintained charge neutrality, assuming cobalt to be present as Co^{2+}, whilst maintaining full occupancy of each site. The fit was similar ($\chi^2=2.787$, $R_{wp}=0.0476$, 31 variables) and suggested that a more accurate description probably lay between these two extremes. The final model therefore allowed oxidation of both cobalt and antimony. Separate constraints were placed on the 4d Co/Sb, and 8h Sb/Pb occupancies to ensure stoichiometry of each site with site constraints on the IDPs. The final fit (Fig. 8, $\chi^2=2.743$, $R_{wp}=0.0472$, 32 variables) is for all atomic coordinates, cell parameters, IDPs and fractional occupancies (excluding oxygen) being refined, where the slightly larger than expected IDPs reflect the disorder due to the random arrangement of cations on the Sb/Pb sites. The refined occupancies (Table 2) imply only minor oxidation of antimony and represent an oxidation state of +2.30 for cobalt, *cf* +2.5 where only cobalt is oxidised. The expansion of *c* and contraction of *a* is modelled in Fig. 9 as a result of the factors mentioned above and reflects a similar trend to that seen on cooling $CoSb_2O_4$ where the Sb–O bonds extend in response to contractions of the octahedral environment and elongation along *c* (Table 3) acting as a buffer to the insertion of larger cations.

Upon cooling to 4 K no change of symmetry was observed and all new reflections were attributed to magnetic ordering of the main phase and impurity. To simplify refinement, the cation occupancies were constrained to values obtained from the 300 K final fit. The refined IDP for the Co/Sb position was slightly negative ($100\times U_{iso}=-0.1(1)$ Å^2), and was therefore constrained at 0.002 Å^2. The final fit (Fig. 10, $\chi^2=2.480$, $R_{wp}=0.0595$, 37 variables,) allowed variation of the lattice parameters, profile coefficients, atomic positions and only the IDPs of oxygen and the constrained Sb/Pb site for the main phase. Two magnetic modes for the main phase were evidenced from indexing the magnetic reflections. The presence of the [1 0 0] at 10.9°2θ and [1 0 1] at 18.6°2θ indicated the presence of C and G modes, respectively; the moment for each mode and orientation was determined as: $C_z=2.86(2)\,\mu_B$ and $G_x=1.65(6)\,\mu_B$ where the magnetic cells had lattice parameters and cation occupancies equal to the main nuclear phase. The Co^{2+} magnetic form factor was adopted. Attempts to refine both magnetic components as one structure were unsuccessful due to the significantly different half widths of the two phases. The G_x mode had visibly broader peaks; which may relate to the difference in length scale for the two types of

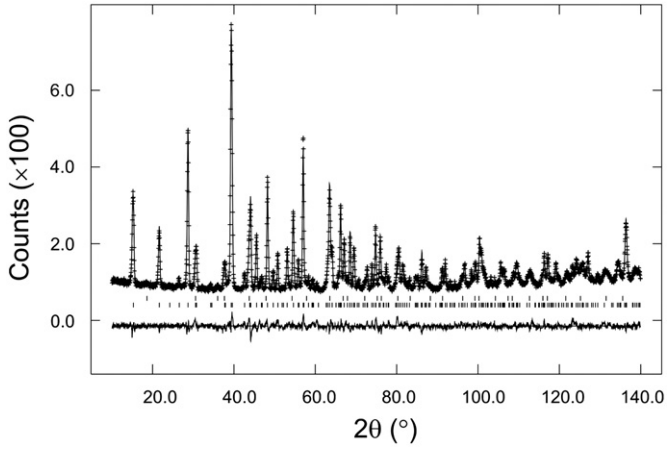

Fig. 8. Final fit for structure refinement of $CoSb_{1.5}Pb_{0.5}O_4$ at 300 K; all IDPs, atomic positions, fractional occupancies (excluding oxygen) and lattice constants have been refined. Fractional occupancies and IDPs of Co/Sb and Sb/Pb were refined as two independent groups.

Table 2
Atomic positions, fractional occupancies, IDPs, statistics and lattice parameters gained from least squares analysis of the NPD data for $CoSb_{1.5}Pb_{0.5}O_4$ at 300 and 4 K.

		$CoSb_{1.5}Pb_{0.5}O_4$	
		300 K	4 K
Co/Sb, 4d	$100\times U_{iso}$ (Å^2)	0.7(2)	0.2[a]
	Occupancy	0.92(2)/0.08(2)	0.92/0.08[a]
Sb/Pb, 8h	(x, y, 0)	0.1613(3), 0.1618(3)	0.1616(3), 0.1618(3)
	$100\times U_{iso}$ (Å^2)	2.38(5)	1.49(5)
	Occupancy	0.74(1)/0.26(1)	0.74/0.26[a]
O1, 8h	(x, y, 0)	0.0962(3), 0.6351(3)	0.0959(3), 0.6355(3)
	$100\times U_{iso}$ (Å^2)	2.04(6)	1.04(7)
O2, 8g	(x, y, 0.25)	0.6746(2), 0.1746(2)	0.6742(2), 0.1742(2)
	$100\times U_{iso}$ (Å^2)	2.65(6)	1.30(6)
χ^2, R_{wp}, R_F^2		2.743, 0.0472, 0.0569	2.480, 0.0595, 0.0645
a/Å		8.4826(2)	8.4727(2)
c/Å		6.0546(2)	6.0494(3)

[a] Parameters fixed during refinement.

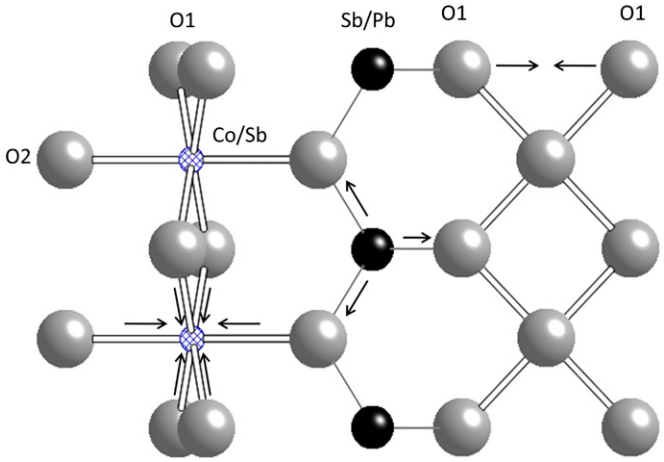

Fig. 9. Influence of lead substitution in $CoSb_2O_4$ on bond lengths and angles. Arrows indicate the direction of the bond length change.

Table 3
Selected interatomic distances (Å) and bond angles (°) from the refined structures.

	$CoSb_2O_4$		$CoSb_{1.5}Pb_{0.5}O_4$	
	300 K	4 K	300 K	4 K
Co/Sb–O1 × 4	2.0710 (9)	2.067 (1)	2.067(2)	2.065 (2)
Co/Sb–O2 × 2	2.151 (1)	2.143 (1)	2.095(2)	2.088(3)
Sb/Pb–O1	1.936 (2)	1.939 (3)	2.069(3)	2.067(4)
Sb/Pb–O2 × 2	1.990 (1)	1.994 (1)	2.056(2)	2.057(2)
O1–Co–O1	88.70 (5)	88.53 (6)	85.81(9)	85.8(1)
O1–Co–O1	166.46 (7)	166.23 (8)	167.0(1)	166.8(1)
O1–Co–O1	92.89 (5)	93.12 (6)	95.66(9)	95.7(1)
Co–O1–Co	91.30 (5)	91.47 (6)	94.19(9)	94.2(1)
O1–Sb–O2	93.25 (6)	93.24 (7)	91.1(1)	91.2(1)
O2–Sb–O2	96.16 (7)	95.88 (8)	94.8(1)	94.7(1)

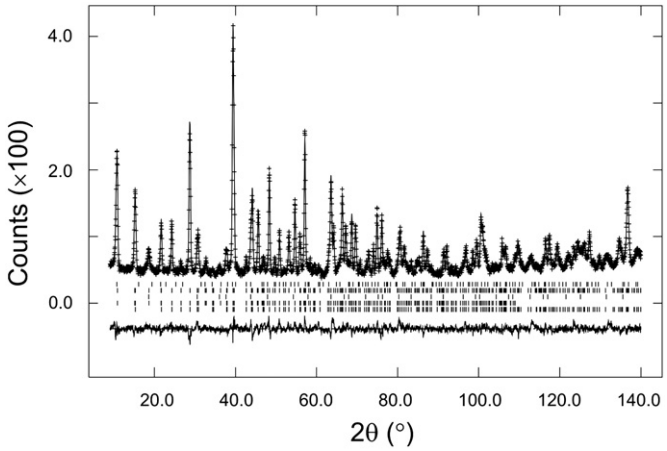

Fig. 10. The final Rietveld refinement of $CoSb_{1.5}Pb_{0.5}O_4$ based on 4 K NPD data using $P4_2/mbc$: observed data (+), calculated and difference profiles (continuous lines) and, from the bottom, reflection positions (|) of $CoSb_{1.5}Pb_{0.5}O_4$ nuclear, C_z, $Co_{2.33}Sb_{0.66}O_4$ nuclear, G_x and $Co_{2.33}Sb_{0.66}O_4$ magnetic structures, respectively.

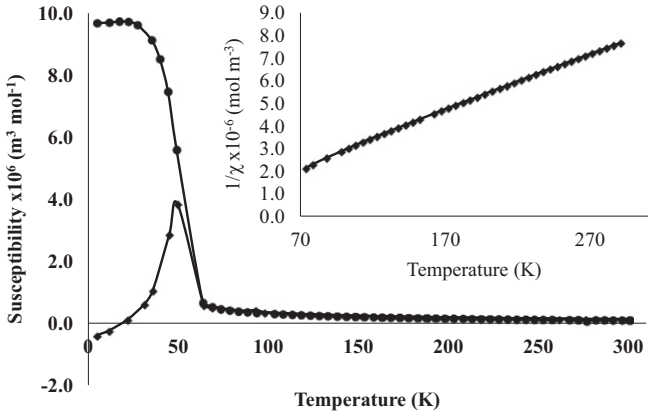

Fig. 11. Magnetic susceptibility data for $CoSb_{1.5}Pb_{0.5}O_4$, FC (●), ZFC (◆); applied field of 100 Oe. Inset: inverse susceptibility from the paramagnetic region 70–300 K.

order, with the G-type order extending over a shorter range. It might be expected that with the similar electronic configurations of Co^{3+} to Fe^{2+} (partially filled t_{2g} orbitals), similarities between magnetic structures would be more apparent, yet the dominant representation of the C_z magnetic component upon oxidation of cobalt suggests the 90° superexchange remains the dominant exchange process. Significant changes in the lattice parameters begin to offer a rationale, where the increase in separation between cobalt sites upon substitution of antimony with lead would further reduce the ability for direct exchange processes to occur resulting in an absence of any A mode. The increase in Co–O1–Co bond angle from 91.47(6)° to 94.2(1)° upon insertion of Pb (at 4 K, Table 3) is consistent with the findings in the lead doped schafarzikite systems yet no G mode was observed. The occurrence of the G mode may relate to the presence of diamagnetic Sb^{5+} within the octahedral chains.

Magnetic susceptibility measurements (Fig. 11) revealed a canted antiferromagnetic ordering of the system similar to that of $CoSb_2O_4$ where a negative response in the ZFC measurements is also observed but to a lesser degree. The magnetic structure surrounding the transition point (T_N=64 K) is significantly different from that of $CoSb_2O_4$ where divergence of the FC and ZFC components occurs at a lower temperature than the transition point indicating further that the oxidation state of cobalt has been modified. The lower ordering temperature compared with $CoSb_2O_4$ ($FeSb_{1.5}Pb_{0.5}O_4$=69 K) [9] suggests that the coupling energy between spins of the magnetic ion sites has been reduced, probably via the diamagnetic Sb^{5+} ions, but is still stronger than the other lead free Schafarzikite systems (T_N=47.0 ± 0.5 and 45 K for $NiSb_2O_4$ [7] and $FeSb_2O_4$ [9], respectively); the increase in magnitude of $\theta = -20.9 \pm 0.6$ K indicates an increase in strength of the spin correlation giving rise to the antiferromagnetic ordering. The calculated moment from the high temperature paramagnetic region ($110 < K > 300$) of the inverse susceptibility plot (Fig. 11 inset) is calculated as 5.08 μ_B per mole, suggesting high spin Co^{3+}.

4. Conclusions

$CoSb_2O_4$ has successfully been synthesised and the magnetic structure is of C-type with ferromagnetic alignment within each octahedral chain of the Schafarzikite structure. The magnetic moments are oriented along [0 0 1] with spins of adjacent chains being antiparallel to give an overall antiferromagnetic arrangement. The system orders at an appreciably higher temperature than its analogues and shows canted antiferromagnetic ordering at T_N=79 K. The change in magnetic order (from A-type to C-type) within the series of MSb_2O_4 Schafarzikites (M=Mn–Zn), therefore occurs between Fe and Co. Attempts to produce lead doped systems have been shown to result in simultaneous oxidation of both Co^{2+} to Co^{3+} and Sb^{3+} to Sb^{5+}.

Acknowledgments

We thank the EPSRC and University of Birmingham for financial support, Emmanuelle Suard for help with the collection of NPD data and Professor Edward Forgan and Dr Elizabeth Blackburn for insightful discussion about the magnetic anomalies. The Bruker D8 diffractometer and the Netzsch STA 449 F1 Jupiter TGA instrument used in this research were obtained through Birmingham Science City: Creating and Characterising Next Generation Advanced Materials (West Midlands Centre for Advanced Materials Project 1), with support from Advantage West Midlands (AWM) and part funded by the European Regional Development Fund (ERDF).

References

[1] J.R. Gavarri, A.W. Hewat, J. Solid State Chem. 49 (1983) 14.
[2] H. Fjellvag, A. Kjekshus, Acta Chem. Scand. Ser. A 39 (1985) 389.
[3] J.A. Gonzalo, D.E. Cox, G. Shirane, Phys. Rev. 147 (1966) 415.
[4] E. Koyama, I. Nakai, K. Nagashima, Nippon Kagaku Kaishi 6 (1979) 793.
[5] J.R. Gavarri, R. Chater, J. Ziolkowski, J. Solid State Chem. 73 (1988) 305.
[6] R. Chater, J.R. Gavarri, A.W. Hewat, J. Solid State Chem. 60 (1985) 78.
[7] H.T. Witteveen, Solid State Commun. 9 (1971) 1313.
[8] A.M. Abakumov, M.G. Rozova, E.V. Antipov, J. Hadermann, G. Van Tendeloo, M.V. Lobanov, M. Greenblatt, M. Croft, E.V. Tsiper, A. Llobet, K.A. Lokshin, Y. Zhao, Chem. Mater. 17 (2005) 1123.
[9] M.J. Whitaker, R.D. Bayliss, F.J. Berry, C. Greaves, J. Mater. Chem. 21 (2011) 14523.
[10] A. Boultif, D. Louer, J. Appl. Crystallogr. 37 (2004) 724.
[11] A.C. Larson, R.B. Von Dreele, General Structural Analysis System (GSAS), Los Alamos National Laboratory, LAUR, 1994. 86-748.
[12] B.H. Toby, J. Appl. Crystallogr. 34 (2001) 210.
[13] I.D. Brown, D. Altermatt, Acta Crystallogr. Sect. B, Struct. Commun. 41 (1985) 244.
[14] J.N. Reimers, J.E. Greedan, C.V. Stager, R. Kremer, J. Solid State Chem. 83 (1989) 20.
[15] B.C. Frazer, P.J. Brown, Phys. Rev. 125 (1962) 1283.
[16] E.G. Puebla, E.G. Rios, A. Monge, I. Rasines, Acta Crystallogr. Sect. B: Struct. Commun. 38 (1982) 2020.
[17] N. Kumar, A. Sundaresan, Solid State Commun. 150 (2010) 1162.
[18] R. Chater, J.R. Gavarri, A.W. Hewat, J. Solid State Chem. 67 (1987) 98.